

# Role of Electrostatic Interactions in Amyloid $\beta$ -Protein ( $A\beta$ ) Oligomer Formation: A Discrete Molecular Dynamics Study

Sijung Yun,\* B. Urbanc,\* L. Cruz,\* G. Bitan,<sup>†</sup> D. B. Teplow,<sup>†</sup> and H. E. Stanley\*

\*Center for Polymer Studies, Department of Physics, Boston University, Boston, Massachusetts; and <sup>†</sup>Department of Neurology, David Geffen School of Medicine, Brain Research Institute and Molecular Biology Institute, University of California, Los Angeles, California

**ABSTRACT** Pathological folding and oligomer formation of the amyloid  $\beta$ -protein ( $A\beta$ ) are widely perceived as central to Alzheimer's disease. Experimental approaches to study  $A\beta$  self-assembly provide limited information because most relevant aggregates are quasi-stable and inhomogeneous. We apply a discrete molecular dynamics approach combined with a four-bead protein model to study oligomer formation of  $A\beta$ . We address the differences between the two most common  $A\beta$  alloforms,  $A\beta_{40}$  and  $A\beta_{42}$ , which oligomerize differently in vitro. Our previous study showed that, despite simplifications, our discrete molecular dynamics approach accounts for the experimentally observed differences between  $A\beta_{40}$  and  $A\beta_{42}$  and yields structural predictions amenable to in vitro testing. Here we study how the presence of electrostatic interactions (EIs) between pairs of charged amino acids affects  $A\beta_{40}$  and  $A\beta_{42}$  oligomer formation. Our results indicate that EIs promote formation of larger oligomers in both  $A\beta_{40}$  and  $A\beta_{42}$ . Both  $A\beta_{40}$  and  $A\beta_{42}$  display a peak at trimers/tetramers, but  $A\beta_{42}$  displays additional peaks at nonamers and tetradecamers. EIs thus shift the oligomer size distributions to larger oligomers. Nonetheless, the  $A\beta_{40}$  size distribution remains unimodal, whereas the  $A\beta_{42}$  distribution is trimodal, as observed experimentally. We show that structural differences between  $A\beta_{40}$  and  $A\beta_{42}$  that already appear in the monomer folding, are not affected by EIs.  $A\beta_{42}$  folded structure is characterized by a turn in the C-terminus that is not present in  $A\beta_{40}$ . We show that the same C-terminal region is also responsible for the strongest intermolecular contacts in  $A\beta_{42}$  pentamers and larger oligomers. Our results suggest that this C-terminal region plays a key role in the formation of  $A\beta_{42}$  oligomers and the relative importance of this region increases in the presence of EIs. These results suggest that inhibitors targeting the C-terminal region of  $A\beta_{42}$  oligomers may be able to prevent oligomer formation or structurally modify the assemblies to reduce their toxicity.

## INTRODUCTION

Alzheimer's disease (AD) is a progressive brain disorder, clinically characterized by the accumulation of extracellular amyloid deposits composed of amyloid  $\beta$ -protein ( $A\beta$ ), intracellular neurofibrillary tangles, and neuronal loss. Recent research supports the hypothesis that cerebral  $A\beta$  accumulation is the primary cause of neurotoxicity in AD (1). Accumulating evidence suggests that  $A\beta$  oligomers and prefibrillar aggregates are the proximal effectors of neurotoxicity in the early stages of AD (2,3). The predominant forms of  $A\beta$  found in brains of AD patients are 40-amino-acids long ( $A\beta_{40}$ ) and 42-amino-acids long ( $A\beta_{42}$ ).  $A\beta_{42}$  is linked particularly strongly with AD. Genetic studies have shown that autosomal dominant forms of AD invariably involve increased production of  $A\beta$  or an increased  $A\beta_{42}/A\beta_{40}$  concentration ratio (4).  $A\beta_{42}$  forms fibrils at significantly higher rates than does  $A\beta_{40}$  (5,6) and  $A\beta_{42}$  self-association produces structures that are more neurotoxic than those formed by  $A\beta_{40}$  (3). Experimentally, there is a distinct difference in oligomerization pathways of  $A\beta_{40}$  and  $A\beta_{42}$  (7). In vitro experiments using the techniques, photo-induced cross-linking of unmodified proteins, size-exclusion chromatography, dynamic light scattering, circular dichroism spectroscopy, and electron

microscopy showed that  $A\beta$  exists as monomers, dimers, trimers, tetramers, and larger oligomers in rapid equilibrium. The  $A\beta_{40}$  oligomer size distribution comprises monomer, dimer, trimer, and tetramer, in similar amounts, and few higher-order oligomers. The  $A\beta_{42}$  distribution is multimodal, displaying a prominent peak of pentamers/hexamers and smaller peaks of dodecamers and octadecamers (7).

Detailed, quantitative analysis of the three-dimensional structures, energetics, and dynamics of oligomer formation are necessary steps toward a molecular understanding of  $A\beta$  assembly and neurotoxicity. During the formation of fibrils, oligomers of different sizes coexist with monomers and larger aggregates such as protofibrils and fibrils (8). The relative amounts of each oligomer type are small, which makes determination of the structural properties of the oligomers difficult. Computer simulations, in contrast, are not subject to the same kinds of problems, allowing small oligomers to be studied at full atomic resolution (for recent reviews, see (9–11)).

Conventional “all-atom” molecular dynamics (all-atom MD) simulations with explicit solvent, which take account of all the protein and solvent atoms, give the most detailed information. However, aggregation studies using all-atom MD with explicit solvent are currently limited to either aggregation of small number of  $A\beta$  fragments such as three  $A\beta(16–22)$  peptides (12) or stability studies of various  $A\beta$  dimers with predetermined structures (13,14). Tarus et al. (13) used a protocol based on shape complementarity to

Submitted September 26, 2006, and accepted for publication January 19, 2007.

Address reprint requests to B. Urbanc, E-mail: brigita@bu.edu.

© 2007 by the Biophysical Society

0006-3495/07/06/4064/14 \$2.00

doi: 10.1529/biophysj.106.097766

determine the initial A $\beta$ <sub>10–35</sub> dimer structure and showed that the peptide dimers are stabilized primarily through hydrophobic interactions. Huet et al. (14) studied A $\beta$ 40 and A $\beta$ 42 dimers and their A21G conformers, starting from their fibrillar conformations and found various possible topologies of dimers in equilibrium. Keeping track of positions and velocities of all the atoms at every time step is computationally expensive. Consequently, the times simulated by the all-atom MD simulations are limited to few microseconds (10). However, protein folding and aggregation usually occur on timescales larger than milliseconds. To overcome this limitation, we use fast and efficient discrete molecular dynamics (DMD) simulations (15) with a simplified four-bead protein model and implicit solvent. DMD is a simplified version of MD using a combination of square-well potentials. The DMD approach with a simplified protein model and implicit solvent increases the efficiency of protein folding and aggregation studies by a factor of  $\sim 10^7$  compared to the all-atom MD (16).

The idea of applying the DMD approach to study protein folding was proposed in 1996 by Zhou et al. (17). Soon after, the method was combined with a one-bead protein model to study folding of a model three-helix bundle protein (18–22). In 2004, Peng et al. (23) used a DMD with two-bead protein model to study aggregation of an ensemble of 28 A $\beta$ 40 peptides into a fibrillar structure. Smith and Hall (24,25) introduced four-bead protein model in combination with the DMD, and showed a cooperative transition of a polyaniline chain into an  $\alpha$ -helical conformation without any a priori knowledge of the native state. Using the four-bead protein model and hydrogen-bond interactions in combination with the DMD on a single 16-residue polyaniline chain, Ding et al. (26) demonstrated a temperature-induced conformational change from the  $\alpha$ -helix to the  $\beta$ -hairpin conformation. Urbanc et al. (27) studied folding and dimer formation using DMD with the four-bead protein model, and investigated stability of dimer conformations predicted by DMD approach using all-atom MD simulations. Lam et al. (28) used the same model to study the A $\beta$ 42 folding and its temperature dependence. The results of Lam et al. were in a good qualitative agreement with an all-atom study using implicit solvent (29) and, importantly, consistent with the temperature dependence of A $\beta$  secondary structure, experimentally determined by Gursky and Aleshkov (30) and Lim et al. (31).

Recently, we studied oligomer formation using a four-bead model with backbone hydrogen-bond interactions and the amino-acid-specific hydrophobic interactions, but no effective electrostatic interactions (EIs) (32). We observed that dimers are the most abundant among the low molecular weight A $\beta$ 40 oligomers and that the frequency of trimers and higher-order oligomers decreases monotonically. In contrast, the A $\beta$ 42 oligomer size distribution was bimodal, with significantly more pentamers than A $\beta$ 40. Multimodal and unimodal oligomer size distributions are discriminating properties of A $\beta$ 42 and A $\beta$ 40, respectively, as observed in vitro by photo-induced cross-linking of unmodified proteins (7).

Experimentally detected pentamer/hexamer A $\beta$ 42 oligomers were termed paranuclei. Existence of A $\beta$ 42 paranuclei and their homotypical assemblies, “oligo-paranuclei”, has been independently confirmed by a combination of ion mobility and mass spectrometry (33). Importantly, paranucleus-like assemblies have been detected in vivo in the form of dodecameric assemblies termed ADDLs (34), globulomers (35), and A $\beta$ \*56 (36). In vitro studies showed that oxidation of M35 blocks A $\beta$ 42 paranucleus formation (37). A $\beta$  without oxidated M35 displays both accelerated (38,39) and delayed (40) fibrillogenesis rate relative to wild-type A $\beta$ . Analysis of intramolecular contacts in A $\beta$ 40 and A $\beta$ 42 pentamers in our in silico study also showed that M35 forms contacts with I41 and A42 in A $\beta$ 42 (32), providing an explanation of the above experimental results (37). In addition, our prior study indicated that A $\beta$ 42 monomers but not A $\beta$ 40 monomers are characterized by a turn structure, centered at G37-G38, and that this turn structure was more prominent in large oligomers (32). This result is consistent with recent proteolysis results using A $\beta$ 40 and A $\beta$ 42 (41).

There is indirect in vitro as well as in silico evidence suggesting that EIs play a significant role in both A $\beta$  folding (41–44) and A $\beta$  fibril formation (45–47). In the present study, we follow the protocols of our previous study (32) using DMD and four-bead protein model with amino-acid-specific interactions (11) to elucidate the role of EIs between pairs of charged amino acids (D, E, K, and R) on folding and oligomerization of A $\beta$ 40 and A $\beta$ 42.

## METHODS

For our simulation method, we use DMD simulations (15). The main simplification in this method is to replace continuous interparticle potentials by a square-well or a combination of square-well potentials. As a result, particles move along straight lines with constant velocities until a pair of particles reaches a distance at which the interparticle potential is discontinuous. A collision event then takes place during which the velocities and directions of the particles are updated while preserving the total kinetic energy, momenta, and angular momenta. Because DMD is event-driven, it is faster than all-atom MD. Our DMD approach using coarse-grained protein models has been described in detail elsewhere (11).

Here we use a four-bead protein model with backbone hydrogen bonding, effective hydrophobic interactions and EIs. We use the four-bead model with hydrogen bonding, introduced by Ding et al. (26), then further generalized by Urbanc et al. (32) to include amino acid-specific hydrophobic and electrostatic interactions. In the four-bead model, the backbone is represented by three beads, corresponding to the amide ( $N$ ), the  $\alpha$ -carbon ( $C_\alpha$ ), and the carbonyl ( $C'$ ) groups. Each side chain is represented by one bead ( $C_\beta$ ). G, which lacks a side chain, has no  $C_\beta$  bead. As the carbonyl oxygen and the amide hydrogen are not explicitly present, an effective backbone hydrogen bond is introduced between the nitrogen atom  $N_i$  of the  $i^{\text{th}}$  amino acid and the carbon atom  $C_j$  of the  $j^{\text{th}}$  amino acid. Because the solvent is not explicitly present in our DMD approach, effective interactions between the side-chain atoms are introduced to mimic the solvent effects. The relative strength of hydrophobic interactions between pairs of side-chain beads is based on the Kyte-Doolittle hydrophobicity scale (48). When two hydrophobic side-chain beads are within the interaction range of 0.75 nm, they interact through a one-step attractive potential. When two hydrophilic side-chain beads are within the same interaction distance, they interact through a one-step repulsive

potential. In our model, the hydrophobic amino acids are A, C, F, L, M, I, and V. The hydrophilic amino acids are D, E, H, K, N, Q, and R. The side chains of the remaining amino acids G, P, S, T, W, and Y interact only through a hard-core repulsion. The EIs are implemented by assigning a two-step potential with two interaction distances, 0.60 nm and 0.75 nm, as described elsewhere (11). When two beads with the same charge are at the interaction distance, they interact through a positive (repulsive) two-step potential. Two oppositely charged beads interact through a negative (attractive) two-step potential.

We set the potential energy of the hydrogen bond,  $E_{\text{HB}}$ , which in proteins is typically in the range 1–5 kcal/mol (49), to unit energy ( $E_{\text{HB}} = 1$ ). We set the potential energy of the hydrophobic interactions  $E_{\text{HP}} = 0.3$ . Experimental free energy of salt bridge formation is estimated to be in the range 0.7–1.7 kcal/mol (50), thus we choose the potential energy of EIs,  $E_{\text{CH}} = 0.6$ . Using the unit of temperature  $E_{\text{HB}}/k_{\text{B}}$  where  $k_{\text{B}}$  is Boltzmann's constant, we estimate that  $T = 0.15$  is appropriate for simulating physiological temperatures. We perform DMD simulations in the canonical ensemble (NVT) using the Berendsen thermostat algorithm (51).

Because we treat the solvent in our DMD approach implicitly, the effective interactions between the side-chain beads include not only protein-protein but also protein-solvent interactions. Thus, there are no generic interaction parameters that would be independent of the environment. Moreover, because different proteins may interact with the solvent in different ways, the implicit effect of the solvent and thus the interaction parameters may depend on the particular protein sequence. The complexity of protein-protein and protein-solvent interactions represents a challenge in protein structure prediction where even the most successful specialized models fail on certain targets (52). The question of how general is a particular choice of interaction parameters in our DMD approach is a topic of future studies.

## RESULTS AND DISCUSSION

We apply the four-bead model with hydrogen-bonding and amino-acid-specific interactions due to hydrophobicity and charge and use DMD with implicit solvent to study  $A\beta_{40}$  and  $A\beta_{42}$  oligomer formation. Due to simplifications in protein description and implicit solvent, our DMD approach is efficient enough to allow for a study of the whole process starting from unfolded separated peptides to formation of quasi-stable  $A\beta$  oligomers with well-defined size distributions. In our protein model, each side chain is replaced by at most one bead, a significant simplification considering side-chain diversity. However, recent developments in understanding of protein folding and assembly show that despite the complexity of the process as a whole, the underlying fundamental physics is simple (53,54). It is believed that the patterns of hydrophobic and hydrophilic residues, rather than the highly specific characters of the individual residues involved, play an important role (55,56). This is consistent with our prior simulation results where we showed that amino-acid-specific interactions due to hydrophobicity itself are sufficient (32) for accounting for the experimentally observed (7) oligomer size distribution differences between  $A\beta_{40}$  and  $A\beta_{42}$ . Here, we apply the same model, with the addition of Coulombic interactions between pairs of charged amino acids, to study the effect of EIs on  $A\beta_{40}$  and  $A\beta_{42}$  oligomer formation.

The primary structure of  $A\beta_{42}$  is DAEFRHDSGYEVHH-QKLVFFAEDVGSNKGAIIGLMVGGVVIA. The primary structure of  $A\beta_{40}$  is identical, except that the last two amino

acids, I and A, are missing. We define the following peptide regions:

1. The N-terminal region D1-K16 (NTR);
2. The central hydrophobic cluster L17-A21 (CHC);
3. The turn A region E22-G29 (TRA);
4. The mid-hydrophobic region A30-M35 (MHR);
5. The turn B region V36-V39 (TRB); and
6. The C-terminal region V40/V40-A42 (CTR). The CTR of  $A\beta_{40}$  consists of only one amino acid, V40.

We simulate eight oligomerization trajectories for  $A\beta_{40}$  and  $A\beta_{42}$  each, starting from spatially separated peptides. Each initial configuration consists of 32  $A\beta_{40}$  ( $A\beta_{42}$ ) peptides with a zero potential energy and with randomized spatial positions and randomized initial velocities of atoms within a cubic box of side 25 nm. The molar concentration is  $\sim 3.4$  mM. This initial setup follows the protocol of our prior publication (32). The concentration in our simulation is 10–100 times higher than that studied experimentally (7). Lowering the concentration is possible only at a high cost of efficiency of our approach. As shown in a recent study by Nguyen and Hall (57), lowering the concentration may give rise to  $\alpha$ -helical aggregates at low temperatures, possibly altering the assembly pathways, a problem to be addressed in future studies.

The energy is in our approach normalized to the potential energy of the hydrogen bond  $E_{\text{HB}} = 1$ . Temperature is expressed in units of energy and also normalized to  $E_{\text{HB}}$ . The maximal potential energy of the hydrophobic/hydrophilic interaction is set to  $E_{\text{CH}} = 0.6/E_{\text{HB}} = 0.6$ . The N-terminal amine group and the C-terminal carboxyl group are noncharged.

Hydrogen bonding is the same for all amino acids and represents the basic interaction needed to model the secondary structure,  $\alpha$ -helix and  $\beta$ -strand, formation. When only the hydrogen-bond interactions are allowed ( $E_{\text{HB}} = 1$ ,  $E_{\text{HP}} = 0$ , and  $E_{\text{CH}} = 0$ ), a single planar  $\beta$ -sheet aggregate is formed (11,27). Thus, only hydrogen-bond interaction is not enough for description of spherical oligomers with only small amounts of secondary structure. Recently, we introduced the effective hydrophobic/hydrophilic interactions, which are amino-acid-specific to mimic the effect of aqueous solution (32). Using the hydrogen bonding and effective hydrophobic interactions but no EIs ( $E_{\text{HB}} = 1$ ,  $E_{\text{HP}} = 0.3$ , and  $E_{\text{CH}} = 0$ ), we found spherical  $A\beta$  aggregates with a dense hydrophobic core and with the hydrophilic N-termini comprising the surface (32).

The aim of the present study is to explore the effects of EIs on oligomer formation of  $A\beta_{40}$  and  $A\beta_{42}$ . The question of how EIs affect the aggregation is intriguing because most of the charged amino acids are at the N-part of the molecule: six of nine charged amino acids are within the D1-K16 fragment as opposed to the hydrophobic residues, which are concentrated in the remaining fragment L17-V40/A42. Fig. 1 shows typical conformations of a folded monomer, dimer, and pentamer of  $A\beta_{42}$  in the absence and presence of EIs.

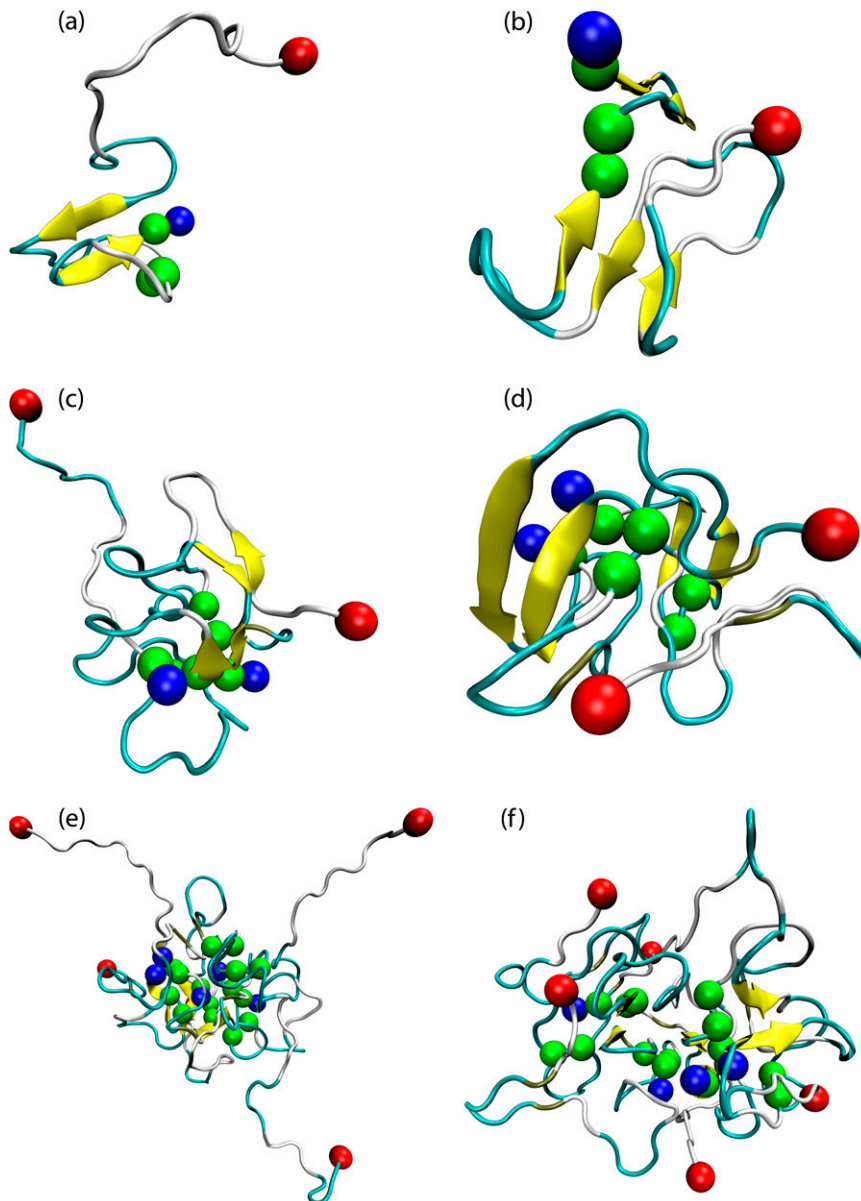


FIGURE 1 Representative conformations of a monomer, dimer, and pentamer of A $\beta$ 42 in the absence ( $E_{CH} = 0$ ) and presence ( $E_{CH} = 0.6$ ) of EIs. A monomer conformation (a) in the absence and (b) presence of EIs. A dimer conformation (c) in the absence and (d) presence of EIs. A pentamer conformation (e) in the absence and (f) presence of EIs. Yellow arrows correspond to the  $\beta$ -strand structure, turns are represented by light blue tubes and random coil-like parts are represented by gray tubes. The N-terminal D1 is marked as a red sphere, and the C-terminal A42 is marked as a blue sphere. I31, I32, and I41, the most hydrophobic residues, are represented as green spheres. This figure is generated by the VMD package (65).

Similar conformations are found in the case of A $\beta$ 40 (data not shown). We observe various topologies at a fixed oligomer size, which is consistent with findings by Huet et al. (14). To gain more quantitative insight into the oligomer formation and structure, we quantify the oligomer size distributions, calculate the intra- and intermolecular contact maps, secondary structure propensities, and Ramachandran plots for each A $\beta$ 40 and A $\beta$ 42 alloform separately.

### A $\beta$ 40 and A $\beta$ 42 oligomer size distributions

All simulations are 10,000,000 simulation steps long. Initially, all the oligomer size distributions are peaked at monomers and the oligomer size distributions of A $\beta$ 40 and A $\beta$ 42 are equivalent. The difference between A $\beta$ 40 and

A $\beta$ 42 size distributions develops steadily with increasing simulation time and at  $\sim 6,000,000$  steps the difference between A $\beta$ 40 and A $\beta$ 42 oligomer size distributions becomes statistically significant as determined by applying the  $\chi^2$ -test (58). When comparing oligomer size distributions of each alloform separately at 8, 8.5, 9, 9.5, and 10 million steps, we find that within this time window size distributions do not differ significantly. However, the number of monomers and oligomers of all sizes is variable. Each of the final oligomer size distributions is obtained by first average over all eight trajectories at a fixed simulation time, and then the resulting ensemble averages are averaged over the simulation times of 8, 8.5, 9, 9.5, and 10 million steps.

We have shown previously that A $\beta$ 40 and A $\beta$ 42 oligomer size distributions in the absence of EIs ( $E_{CH} = 0$ ) are

significantly different (Fig. 2 *a*) (32).  $A\beta_{40}$  and  $A\beta_{42}$  oligomer size distributions in the presence of EIs ( $E_{CH} = 0.6$ ) are significantly shifted toward larger oligomers, as shown in Fig. 2 *b*. Comparing the  $A\beta_{40}$  and  $A\beta_{42}$  oligomer size distributions by applying the  $\chi^2$ -test, we conclude that in the presence of EIs, the distributions are significantly different ( $p < 0.01$ ).

In the presence of EIs, the average size of  $A\beta_{40}$  oligomers increases from 3.0 to 5.2 molecules, and the average size of  $A\beta_{42}$  oligomers increase from 3.7 to 6.2 molecules. These results suggest that EIs facilitate aggregation.  $A\beta_{42}$  forms significantly more nonamers and larger oligomers compared to  $A\beta_{40}$ . The  $A\beta_{40}$  size distribution is unimodal with a peak at tetramers. The  $A\beta_{42}$  distribution contains a trimer peak and two additional peaks, at  $n = 9$  (nonamer) and  $n = 14$  (tetradecamer), neither of which is present in the  $A\beta_{40}$  distribution. A multimodal oligomer size distribution was observed experimentally with  $A\beta_{42}$ , but not with  $A\beta_{40}$  (7).

In our simulations, the N- and C-termini are uncharged, whereas in the experimental studies, the N-terminus is positively charged ( $NH_3^+$ ) and the C-terminus is negatively charged ( $COO^-$ ) (7,42). Observation of high-order oligomers in our simulations is consistent with in vitro results in which the C-terminal carboxyl group was replaced by the

electrostatically neutral carboxamide, resulting in a greater abundance of high molecular weight oligomers (42). Our simulation results, in combination with experimental findings, thus suggest that inclusion of charged termini, in particular the C-terminal negative charge, will moderate formation of  $A\beta$  oligomers. This hypothesis will be tested in future computational and experimental studies.

## Secondary structure of $A\beta$ monomers

We calculate the secondary structure propensities on each folded monomer separately using the STRIDE program (59) and then average over different conformations to obtain the average values of the  $\alpha$ -helix, turn, and  $\beta$ -strand propensities per amino acid. At 1,000,000 (M) step, the potential energy of individual monomers is stabilized (data not shown), thus we consider monomers to be in a folded state at 1 M step.

Folded monomers do not have a significant amount of  $\alpha$ -helix structure (data not shown). Fig. 3, *a* and *b*, show the turn propensity per amino acid for folded  $A\beta_{40}$  and  $A\beta_{42}$  monomers in the absence and presence of EIs. A dramatic effect of EIs on the turn propensities in both alloforms is observed in the region A21-A30. In the absence of EIs this region is characterized by two turns, the first at A21-V24 and the second at S26-G29. In the presence of EIs, only a single turn within the region V24-G29 remains.

Fig. 3, *c* and *d*, show the  $\beta$ -strand propensity per amino acid for folded  $A\beta_{40}$  and  $A\beta_{42}$  monomers in the absence and presence of EIs. As a result of EIs in both alloforms, the regions A21-D23 and K28-I31 show an increased  $\beta$ -strand propensity. In  $A\beta_{40}$  monomers the regions A2-F4 and L34-G38 show a decreased  $\beta$ -strand propensity due to EIs. In  $A\beta_{42}$  monomers the regions R5-H6 and L34-V39 show a slightly decreased  $\beta$ -strand propensity due to EIs. Notice that the  $\beta$ -strand propensity per amino acid is  $<40\%$  for  $A\beta_{40}$  and  $<30\%$  for  $A\beta_{42}$ . The number of turns and consequently also the number of  $\beta$ -strand regions in the  $A\beta_{42}$  monomer (5) is bigger than in the  $A\beta_{40}$  monomer (4), indicating a more compact structure of the  $A\beta_{42}$  monomer as compared to the  $A\beta_{40}$  monomer, a consequence of a strongly hydrophobic CTR in  $A\beta_{42}$ , which introduces an additional turn centered at G37-G38. The average turn and  $\beta$ -strand contents of  $A\beta_{40}$  and  $A\beta_{42}$  folded monomers are displayed in Table 1. These contents are calculated from propensities per residue by averaging over all residues in the peptide. Table 1 shows that for both  $A\beta_{40}$  and  $A\beta_{42}$  the average turn content is in the range 43–45% while the average  $\beta$ -strand content is in the range 10–12%. Neither the average turn nor the average  $\beta$ -strand content is strongly affected by EIs.

The above results suggest that even in the presence of EIs, the  $A\beta$  monomer is a collapsed coil with several turns and some  $\beta$ -strand but no  $\alpha$ -helical structure, which is in agreement with existing experimental studies (30,41,60). The  $\beta$ -strand propensity of  $A\beta_{40}$  monomer as shown in Fig. 3 *c* is also consistent with a recent study of  $A\beta_{40}$  folding

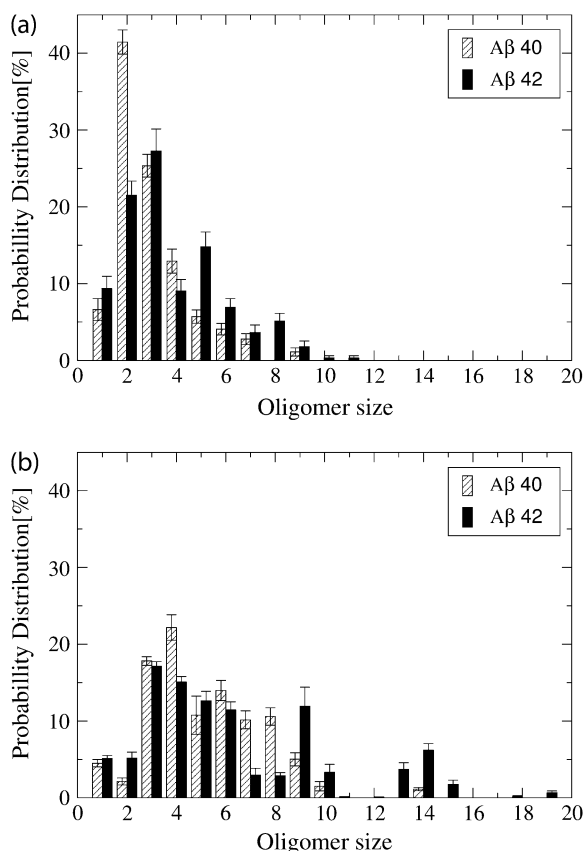


FIGURE 2 Oligomer size distributions of  $A\beta_{40}$  and  $A\beta_{42}$  at (a)  $E_{CH} = 0$  and (b)  $E_{CH} = 0.6$ . All size distributions are averages over the time frames at 8, 8.5, 9, 9.5, and 10 million simulation steps.

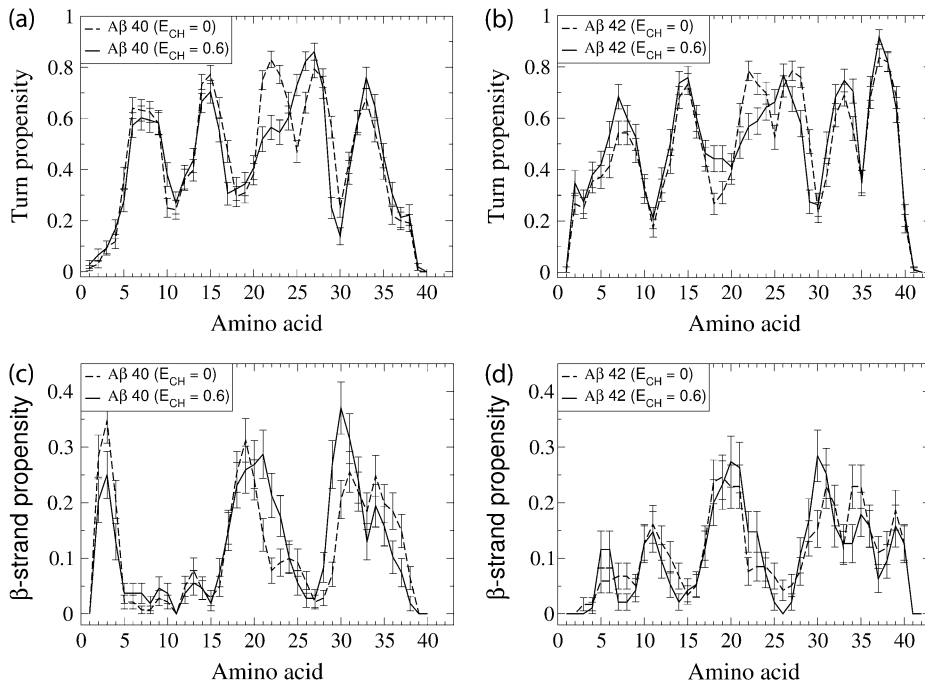


FIGURE 3 The effect of EIs on turn and  $\beta$ -strand propensities per residue in folded A $\beta$  monomers in the absence and presence of EIs. Turn propensities of (a) A $\beta$ 40 and (b) A $\beta$ 42 monomers.  $\beta$ -strand propensities of (c) A $\beta$ 40 and (d) A $\beta$ 42 monomers.

using a scanning tunneling microscopy that showed monomers folded into three or four domains with some  $\beta$ -strand structure (61).

### Intramolecular contacts of folded A $\beta$ monomers

Here we discuss the effect of EIs on the intramolecular contacts among pairs of amino acids of folded monomers. Initially, monomer peptides are in zero-potential energy (unfolded) conformations. At 0.1 M steps, over 60% of peptides (65.9% for A $\beta$ 40, 60.5% for A $\beta$ 42) are folded. We describe the regions of the most important contacts between pairs of amino acids. We first describe “short-range” contacts formed within the regions TRB, MHR, and TRA. Then, we describe the “long-range” contacts between the regions CHC-CTR, CHC-MHR, and CHC-NTR.

Previous results (32) showed that while A $\beta$ 40 and A $\beta$ 42 monomers both display strong contacts within the TRA region, strong contact in the TRB region with a turn centered at G37-G38 are characteristic of A $\beta$ 42 only. This *in silico* difference between A $\beta$ 40 and A $\beta$ 42 folding is consistent with experimental findings by Lazo et al. (41).

**TABLE 1** Average turn and  $\beta$ -strand propensities per residue with standard errors within folded A $\beta$ 40 and A $\beta$ 42 monomers

	A $\beta$ 40		A $\beta$ 42	
	$E_{CH} = 0$	$E_{CH} = 0.6$	$E_{CH} = 0$	$E_{CH} = 0.6$
Turn	$0.44 \pm 0.04$	$0.43 \pm 0.04$	$0.48 \pm 0.04$	$0.50 \pm 0.05$
$\beta$ -strand	$0.11 \pm 0.02$	$0.12 \pm 0.03$	$0.11 \pm 0.03$	$0.10 \pm 0.03$

Each value is an average of over 100 monomer conformations after 1,000,000 simulation steps.

In Fig. 4, we compare the intramolecular contact maps of A $\beta$ 40 and A $\beta$ 42 in the presence and absence of EIs. Fig. 4 shows the region containing the strongest contact V36-V39 as reported in our previous study (rectangle 1 in Fig. 4, a and c) (32). In A $\beta$ 40 the contacts between the amino-acid regions L34-V36 and V39-V40 are significantly weaker than similar contacts between L34-V36 and V39-A42 in A $\beta$ 42. EIs do

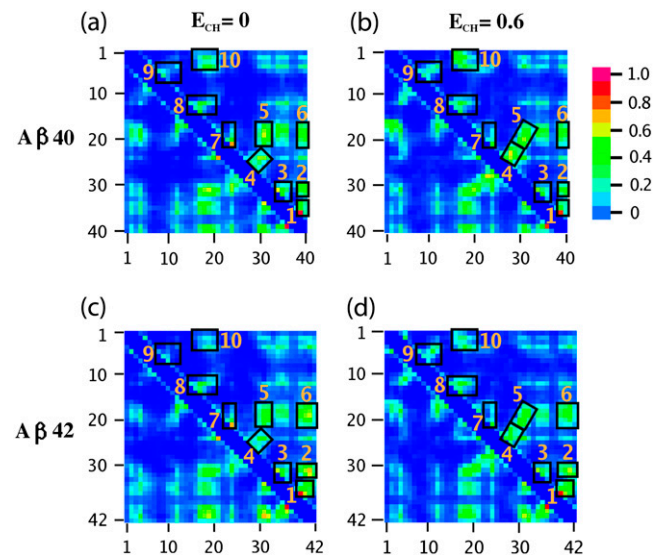


FIGURE 4 Intramolecular contact maps of folded A $\beta$ 40 and A $\beta$ 42 monomers at  $E_{CH} = 0$  (left column) and  $E_{CH} = 0.6$  (right column). The strength of the contact map is color-coded following the rainbow scheme: from blue (no contacts) to red (the largest number of contacts). Each contact map is an average of over 100 monomer conformations after 1,000,000 simulation steps.

not affect contacts in the TRB region (*rectangle 1* in Fig. 4, *b* and *d*). This result suggests that EIs do not alter the contacts that contribute to differences between A $\beta$ 40 and A $\beta$ 42 folding in the CTR.

A few important contacts in both alloforms in the MHR, concentrated around the strongest contact I31-L34, bring into proximity the two MHR regions A30-I32 and L34-V36 and are not affected by EIs (*rectangle 3* in Fig. 4, *a-d*). The formation of these contacts within the MHR is promoted by G33 because glycines are typically associated with a high turn/loop propensity. Contacts between the CTR and MHR are present in both A $\beta$ 40 (*rectangle 2* in Fig. 4 *a*) and A $\beta$ 42 (*rectangle 2* in Fig. 4 *c*), but are significantly stronger in A $\beta$ 42. These contacts are not affected significantly by EIs (*rectangle 2* in Fig. 4, *b* and *d*).

The central and most abundant contacts in folded monomers of both alloforms are formed as a consequence of the formation of the turn involving the TRA region (*rectangles 4* and *7* in Fig. 4, *a-d*). The TRA region contains charged amino acids E22, D23, and K28, thus it is expected that EIs will influence the contacts in this region. A strong contact A21-V24 in the TRA region becomes weaker as a result of EIs (*rectangle 7* in Fig. 4, *a-d*), which is consistent with the effect of EIs on the turn propensity in this region, changing a two-turn region into a one-turn region. Formation of contacts within the TRA brings into proximity the CHC and MHR (*rectangle 5* in Fig. 4, *a-d*). In both alloforms in the absence of EIs, the CHC region makes contacts with the MHR with F19-I31 as the strongest contact (*rectangle 5* in Fig. 4, *a* and *c*). EIs enhance the contacts within and around the TRA region in both alloforms, making contacts between the regions L17-D23 and K28-I32 (*rectangle 5* in Fig. 4, *b* and *d*) stronger. This enhanced feature is a consequence of a salt bridge formation between the oppositely charged D23 and K28. The TRA region was recently hypothesized to represent the nucleation region of A $\beta$  folding (41). This turn has been shown to be important in the fibril structure (45,46), suggesting that this region maintains conformational stability throughout the folding and assembly of A $\beta$ . Our results are consistent with this hypothesis as they show that formation of contacts within the TRA region induces prominent contacts between the CHC and MHR, resulting in the highest concentration of intramolecular contacts, involving the TRA, CHC, and MHR.

In the absence of EIs, the MHR region A30-M35 makes contacts with both the CHC (*rectangle 5* in Fig. 4, *a-d*) and CTR (*rectangle 2* in Fig. 4, *a-d*). These contacts do not change significantly in the presence of EIs. The difference between A $\beta$ 40 and A $\beta$ 42 is that in A $\beta$ 40 contacts between the regions A30-I32 and L34-V36 are stronger than the contacts between A30-I35 and V39-V40, while in A $\beta$ 42 the contacts between the regions A30-I35 and V39-A42 are dominant. This result suggests that in A $\beta$ 42 folding the CTR plays a prominent role, while in A $\beta$ 40 the contacts within the MHR and between MHR and CHC regions are more important.

The contacts between the K16-F19 and E11-H14 become more pronounced in the presence of EIs due to the EI between the negatively charged E11 and positively charged K16 (*rectangle 8* in Fig. 4, *a-d*). A weaker group of contacts within the NTR between F4-H6 and Y10-V12 is a result of a turn centered at D7-G9 and hydrophobic attraction F4-V12. These contacts are very weak in the absence of EIs (*rectangle 9* in Fig. 4, *a* and *c*) but become stronger in the presence of EIs due to salt bridge R5-E11 (*rectangle 9* in Fig. 4, *b* and *d*).

Long-range contacts between V39-V40 and CHC are observed in both A $\beta$ 40 and A $\beta$ 42 in the absence of EIs (*rectangle 6* in Fig. 4, *a* and *c*). These contacts remain strong in the presence of EIs (*rectangle 6* in Fig. 4, *b* and *d*). In A $\beta$ 42, these contacts are stronger than in A $\beta$ 40, both in the absence and presence of EIs. Another region of long-range contacts is observed in both alloforms between the K16-F20 and D1-F4 in the absence of EIs (*rectangle 10* in Fig. 4, *a* and *c*). These contacts become more pronounced in the presence of EIs due to electrostatic attraction between the negatively charged D1 and E3 and positively charged K16 (*rectangle 10* in Fig. 4, *b* and *d*). The long-range contacts between CTR and A2-F4, and MHR and A2-F4 are also present in both A $\beta$ 40 and A $\beta$ 42 but are weaker than the others and are not significantly influenced by EIs.

### Time progression of A $\beta$ folding events

Fig. 5 shows time evolution of A $\beta$ 40 and A $\beta$ 42 monomer folding events in the presence of EIs. Initially, A $\beta$ 40 and A $\beta$ 42 monomers are in zero potential energy, random coil conformations. At 1000 simulation steps, contacts are formed between L34-V36 and CTR in both A $\beta$ 40 and A $\beta$ 42. However, only in A $\beta$ 42, these contacts are associated with a turn structure in the TRB region as described in the previous section. At 2000 steps, the contacts between regions CHC and TRA, CHC and MHR, CHC and CTR develop in both A $\beta$ 40 and A $\beta$ 42. These contacts are associated with a turn structure in the TRA region in both A $\beta$ 40 and A $\beta$ 42. At 4000 steps, contacts between NTR and CHC develop in A $\beta$ 40. At 8000 steps, as the contacts between NTR and CHC in A $\beta$ 40 are more pronounced, these contacts also emerge in A $\beta$ 42. At 0.1 M steps, the long-range contacts between NTR and CTR are formed in both A $\beta$ 40 and A $\beta$ 42. Using the regions defined in Fig. 4, *b* and *d*, the time progression of contacts follows the numbering 1, 2, 3, ... 10, i.e., A $\beta$  folding starts at the C-terminal and progresses toward the N-terminal. In A $\beta$ 40, the turn structure in the TRA region is the first structural element that is formed in the process of folding, supporting the hypothesis of Lazo et al. (41) stating that the region 21–30 nucleates A $\beta$ -folding. However, in A $\beta$ 42 the turn structure in the TRB region is formed before the formation of the turn structure in the TRA region. This result suggests that in A $\beta$ 42 the TRB region nucleates the folding before formation of contacts in the TRA region.

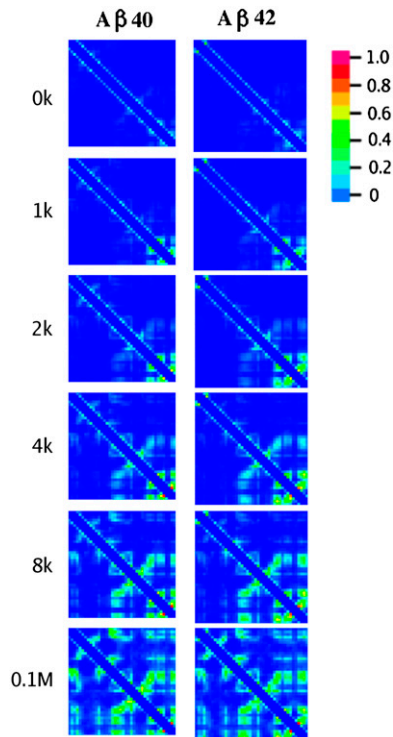


FIGURE 5 Detailed time evolution of intramolecular contact formation during A $\beta$ 40 (left column) and A $\beta$ 42 folding (right column). The strength of the contact map is color-coded as in Fig. 4. Each contact map is an average of over 100 monomer conformations.

### Secondary structure of A $\beta$ pentamers and larger oligomers

In our previous work (32), we reported the secondary structure difference between A $\beta$ 40 and A $\beta$ 42 pentamers that can be found in the NTR and CTR. A $\beta$ 42 pentamers displayed an increased  $\beta$ -strand propensity at the V39-I41, while A $\beta$ 40 pentamers showed an increased  $\beta$ -strand propensity at the A2-F4. Our present data show that these differences remain intact in the presence of EIs.

Pentamers and larger oligomers do not have any significant amount of  $\alpha$ -helix structure (data not shown). Fig. 6, *a* and *b*, show the turn propensity per amino acid for A $\beta$ 40 and A $\beta$ 42 pentamers and larger oligomers in the absence and presence of EIs. EIs do not affect the turn propensity significantly. In A $\beta$ 42, a slight increase in the turn propensity due to EIs is found in the region R5-Y10.

Fig. 6, *c* and *d*, shows the  $\beta$ -strand propensity per amino acid for A $\beta$ 40 and A $\beta$ 42 pentamers and larger oligomers. In both alloforms, the  $\beta$ -strand propensity in the region K28-I31 slightly increases and in the region L34-G38 decreases due to EIs. In the presence of EIs, the  $\beta$ -strand propensity in the CHC increases in A $\beta$ 40, while it decreases in A $\beta$ 42 pentamers and larger oligomers.

We also calculate the average turn and  $\beta$ -strand contents within A $\beta$ 40 and A $\beta$ 42 pentamers and larger oligomers in

the absence and presence of EIs. The data is shown in Table 2. The average contents are calculated from propensities per residue by averaging over all residues in the peptide. The average turn content is in the range 41–45% and the average  $\beta$ -strand content is in the range 11–13%. There is no significant difference between the two alloforms and no significant effect due to EIs.

These results show that pentamers and larger oligomers in our study have a globular structure dominated by turns and loop and some  $\beta$ -strand propensity. EIs change the relative  $\beta$ -strand propensities of some regions, but do not affect significantly the overall secondary structure.

### Ramachandran plots of selected amino acids within the A $\beta$ 42 pentamers and higher oligomers

Because our protein model as well as the interactions is simplified, we tested A $\beta$ 42 oligomer conformers by calculating the Ramachandran plots. We selected the following 10 amino acids from different regions of the protein: D1, Y10, F19, E22, D23, S26, K28, M35, I41, and A42.

Our results shown in Fig. 7 indicate that both in the absence and presence of EIs, the most populated ( $\Phi$ ,  $\Psi$ ) region corresponds to the  $\beta$ -sheet region. The exceptions are D1 and A42, the N- and C-terminal amino acids, due to an increased flexibility at the two termini, and E22. Interestingly, E22 shows a substantially higher propensity to form a right-handed  $\alpha$ -helix. Our results show that EIs do not affect these plots in a significant way. These results are in qualitative agreement with A $\beta$  dimer analysis of Huet et al. (14), who studied A $\beta$  dimer conformations by all-atom MD, suggesting that our four-bead model yields relatively realistic set of  $\Phi$  and  $\Psi$  angles and thus adequately accounts for the protein backbone structure.

### Tertiary structure of pentamers and larger oligomers

The tertiary structure of A $\beta$  molecules within pentamers and larger oligomers (Fig. 8) is highly reminiscent of the structure of individual monomers (compare Figs. 4 and 8), suggesting that no major refolding events are needed in monomers before oligomer formation. However, there is less involvement of the N-terminal amino acids and more intramolecular contacts involving the C-terminal amino acids in A $\beta$  molecules comprising pentamers and larger oligomers of both alloforms.

There are significant differences between A $\beta$ 40 and A $\beta$ 42 intramolecular contact maps of pentamers and larger oligomers. The differences between A $\beta$ 40 and A $\beta$ 42 in the absence of EIs have been described in our previous work (32) and can be observed comparing the relative importance of the CHC and CTR: in A $\beta$ 42 the contacts of CTR with MHR and CHC are dominant, while in A $\beta$ 40 the CHC plays a dominant role. In A $\beta$ 40 (Fig. 8, *a* and *b*) the contacts in

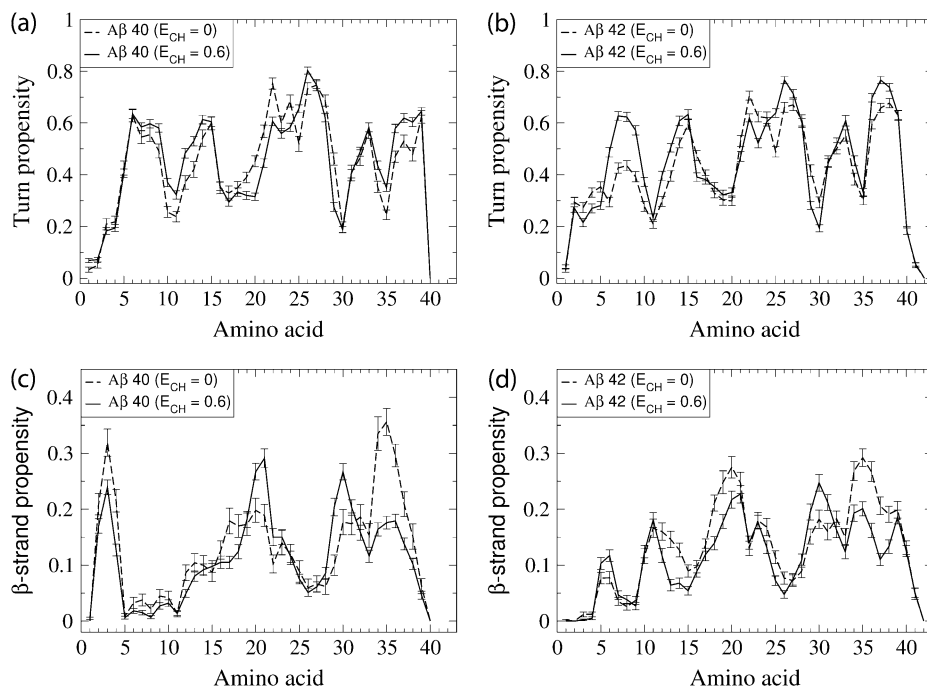


FIGURE 6 The effect of EIs on turn and  $\beta$ -strand propensities per residue within  $A\beta$  pentamers and larger oligomers in the absence and presence of EIs. Turn propensities of (a)  $A\beta$ 40 and (b)  $A\beta$ 42 pentamers and larger oligomers.  $\beta$ -strand propensities of (c)  $A\beta$ 40 and (d)  $A\beta$ 42 pentamers and larger oligomers.

regions marked by rectangles 1, 3, 4, and 5 get weaker due to EIs, while the opposite is true in  $A\beta$ 42 (Fig. 8, *c* and *d*), where the contacts within the rectangles 1, 2, 3, 4, and 5 get stronger. This effect of EIs on the intramolecular contacts can only be observed in pentamers and larger oligomers and not in unassembled monomers.  $A\beta$ 42 pentamers and larger oligomers, in the presence of EIs, have significantly stronger intramolecular contacts than  $A\beta$ 40, suggesting that  $A\beta$ 42 pentamers and larger oligomers are intrinsically more stable than their  $A\beta$ 40 counterparts.

Fig. 7 shows Ramachandran scattering plot on pentamers and larger oligomers of  $A\beta$ 42. As seen from contact map analysis, in the presence of EIs, D1s are more populated in  $\beta$ -sheet region, which is the upper left corner.

### Quaternary structure of pentamers and larger oligomers

Intermolecular contact maps indicate contacts among different  $A\beta$  molecules within an oligomer that are most important in oligomer formation. Previously, we showed that in  $A\beta$ 40

pentamers, pairs of the CHC regions show the highest propensity to interact, whereas in  $A\beta$ 42 pentamers the most frequent contacts are between the CTR of one peptide and the CHC and MHR of the other (32). That result indicated that the CTRs are critically involved in aggregation of  $A\beta$ 42 but not  $A\beta$ 40.

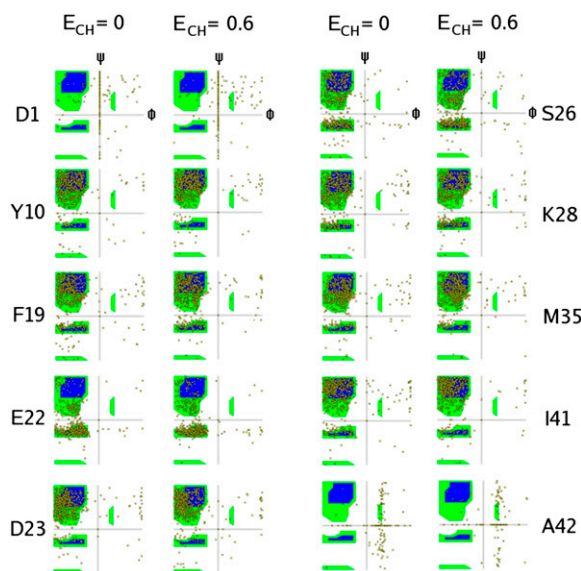


FIGURE 7 Ramachandran plots of  $A\beta$ 42 pentamers and larger oligomers for selected residues D1, Y10, F19, E22, D23, S26, K28, M35, I41, and A42 in the absence and presence of EIs. Horizontal and vertical axes correspond to the angles  $\Phi$  and  $\Psi$ , respectively, both varying from  $-180^\circ$  to  $180^\circ$ . Each plot contains  $\sim 640$  points corresponding to  $A\beta$ 42 pentamers to decamers obtained at 8, 8.5, 9, 9.5, and 10 million simulation steps. Ramachandran plots are generated using the VMD software package (65).

**TABLE 2** Average turn and  $\beta$ -strand propensities per residue with standard errors within  $A\beta$ 40 and  $A\beta$ 42 pentamers and larger oligomers

	$A\beta$ 40		$A\beta$ 42	
	$E_{CH} = 0$	$E_{CH} = 0.6$	$E_{CH} = 0$	$E_{CH} = 0.6$
Turn	$0.44 \pm 0.02$	$0.45 \pm 0.02$	$0.42 \pm 0.02$	$0.45 \pm 0.02$
$\beta$ -strand	$0.13 \pm 0.02$	$0.11 \pm 0.01$	$0.13 \pm 0.01$	$0.11 \pm 0.01$

Each value is an average of over 50 conformations at 8, 8.5, 9, 9.5, and 10 million simulation steps.

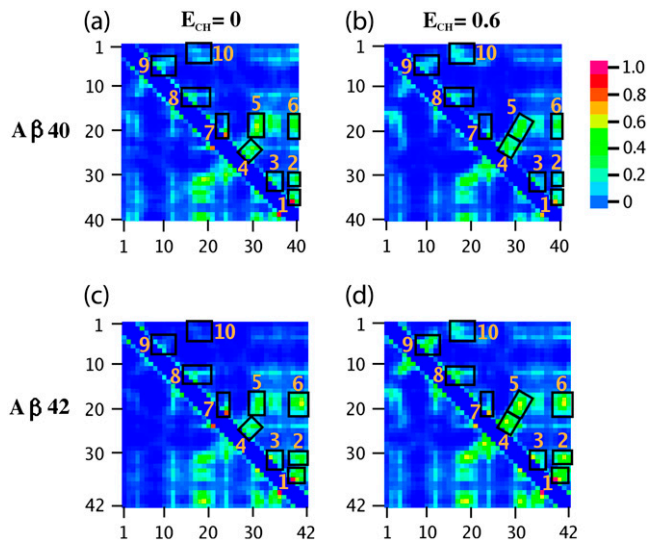


FIGURE 8 Intramolecular contact maps of A $\beta$ 40 and A $\beta$ 42 pentamers and larger oligomers at  $E_{CH} = 0$  and  $E_{CH} = 0.6$ . Each contact map is an average of >50 conformations obtained at 8, 8.5, 9, 9.5, and 10 million simulation steps.

Fig. 9 shows intermolecular contact maps of pentamers and larger oligomers of A $\beta$ 40 and A $\beta$ 42 in the absence (Fig. 9, *a* and *c*) and presence (Fig. 9, *b* and *d*) of EIs. Perhaps the most surprising overall observation is that the intermolecular contacts that involve the CHC, i.e., contacts between pairs of CHCs (rectangle 3 in Fig. 9, *a–d*), between the CHC and MHR (rectangle 5 in Fig. 9, *a–d*), and between the CHC and CTR (rectangle 6 in Fig. 9, *a–d*), become weaker as a consequence of EIs in both alloforms, but this weakening is more pronounced in A $\beta$ 40 oligomers. This weakening of the

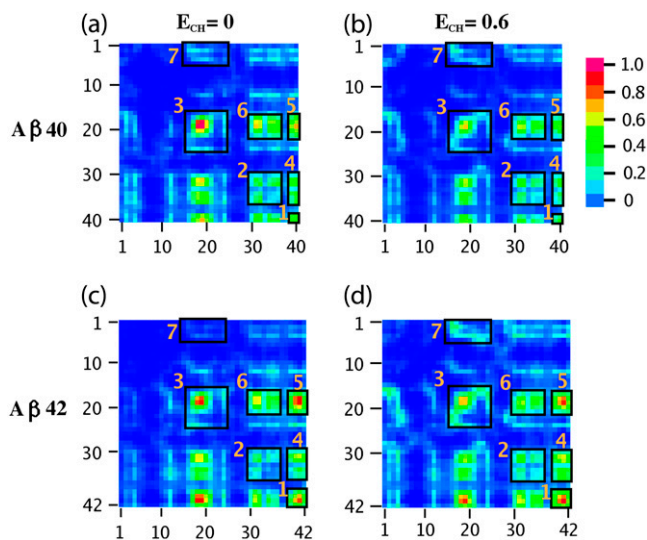


FIGURE 9 Intermolecular contact maps of A $\beta$ 40 and A $\beta$ 42 pentamers and larger oligomers at  $E_{CH} = 0$  and  $E_{CH} = 0.6$ . Each contact map is an average of >50 conformations at 8, 8.5, 9, 9.5, and 10 million simulation steps.

contacts involving the CHC due to EIs is surprising because the CHC is surrounded by charged residues (K16, E22, and D23). Thus, we would expect CHCs to interact pairwise in an antiparallel fashion to maximize the mutual attraction involving hydrophobic residues by additional salt bridge formation and thus minimize the free energy. Instead, our results show that EIs weaken the contacts between pairs of CHCs. We also showed that EIs promote formation of larger oligomers in both A $\beta$ 40 and A $\beta$ 42. These two results combined imply that weakening of the contacts between pairs of CHCs in A $\beta$ 40 oligomers might actually indirectly promote aggregation into larger oligomers.

The only exception to the above observation is the region between D1-R5 and K16-D23, which is rather weak in both alloforms in the absence of EIs, but gets more pronounced in particular in A $\beta$ 42 due to EIs (rectangle 7 in Fig. 9, *a–d*).

Our results indicate important differences in the way EIs affect A $\beta$ 40 and A $\beta$ 42 oligomers. In A $\beta$ 40 oligomers the intermolecular contacts between pairs of CTRs (rectangle 1 in Fig. 9, *a* and *b*), between pairs of MHRs (rectangle 2 in Fig. 9, *a* and *b*), and between the CTR and MHR (rectangle 4 in Fig. 9, *a* and *b*) remain unaffected by EIs. In A $\beta$ 42 oligomers, on the other hand, the intermolecular contacts in these same regions get stronger even though that part of A $\beta$ 42 (MHR and CTR) is free of charge and thus EIs would not be expected to make a difference. The strongest increase in the intermolecular contact intensity in A $\beta$ 42 oligomers is between pairs of CTRs (rectangle 1 in Fig. 9, *b* and *d*) and the second strongest is between the CTR and MHR (rectangle 4 in Fig. 9, *b* and *d*). Thus, in A $\beta$ 42 oligomers the contacts involving the CHCs get weaker and the contacts involving the CTRs get stronger due to EIs, resulting in a significantly larger oligomers. These results suggest that in A $\beta$ 42 the CTRs are most important for intermolecular assembly into pentamers and larger oligomers. The lack of strong intermolecular contacts involving CTRs in A $\beta$ 40 suggests that the CTRs are also the main source of the differences between A $\beta$ 40 and A $\beta$ 42 oligomer formation. Recently, the importance of the intermolecular CHC contacts in A $\beta$ 40 versus the intermolecular CTR contacts in A $\beta$ 42 was observed experimentally by Maji et al. (62), in agreement with our present in silico results, suggesting the biological relevance of our DMD approach, which is able to capture the essential differences between A $\beta$ 40 and A $\beta$ 42 oligomerization.

### Intra- and intermolecular hydrogen bonds in pentamers and larger oligomers

Here we address the question of how much hydrogen bonds contribute to intra- and intermolecular contacts in pentamers and larger oligomers. We first calculate the probabilities for forming an intra- or intermolecular hydrogen bond per amino acid. The amino acids that are most hydrogen-bond active are shown in Tables 3 and 4. Our results show that even for

**TABLE 3 Average hydrogen bond propensities per residue, showing the five most frequent residues involved in intramolecular hydrogen bonding within A $\beta$ 40 and A $\beta$ 42 pentamers and larger oligomers**

A $\beta$ 40				A $\beta$ 42			
$E_{CH} = 0$		$E_{CH} = 0.6$		$E_{CH} = 0$		$E_{CH} = 0.6$	
L17	0.17	M35	0.14	V40	0.17	A30	0.17
A21	0.15	G38	0.14	I31	0.16	G29	0.15
G33	0.15	I31	0.13	G38	0.15	E11	0.15
V24	0.14	G33	0.12	A21	0.13	R5	0.14
G38	0.14	G37	0.12	G29	0.13	I31	0.14

Each value is an average of over 50 conformations at 8, 8.5, 9, 9.5, and 10 million simulation steps.

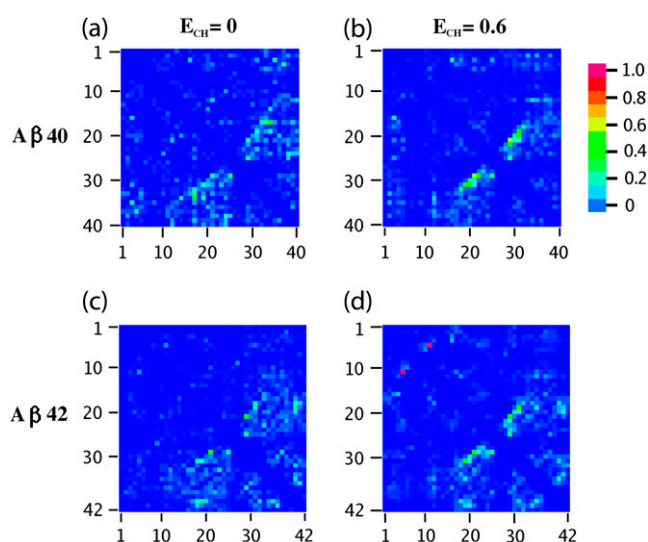
the amino acids that are most likely to form hydrogen bonds, probabilities are  $<0.20$ . The sum of intra- and intermolecular probabilities per amino acid does not exceed 0.30/0.40, which is consistent with the  $\beta$ -strand propensity per amino acid (Fig. 6).

Fig. 10 shows the intramolecular hydrogen bond contacts of A $\beta$ 40 (Fig. 10, *a* and *b*) and A $\beta$ 42 (Fig. 10, *c* and *d*) pentamers and larger oligomers in the absence (Fig. 10, *a* and *c*) and presence (Fig. 10, *b* and *d*) of EIs. These intramolecular hydrogen bond maps are normalized to the highest value of intramolecular hydrogen-bond formation probability, which is  $<0.09$ . The regions with the highest amount of hydrogen bonds can be found between the regions K16-V24 and K28-V40. In A $\beta$ 42 oligomers some additional hydrogen bonds are formed between the MHR and CTR and between the CHC and CTR. EIs increase the hydrogen-bond probabilities within the TRA region and between the CHC and MHR due to salt bridge D23-K28. This effect is more pronounced in A $\beta$ 40. Interestingly, the strongest intramolecular hydrogen bond occurs in A $\beta$ 42 oligomers between F4 and V12, possibly stabilized by proximity of oppositely charged R5 and E11. Why this same hydrogen bond is missing in A $\beta$ 40 oligomers may be understood by observation that in A $\beta$ 40 the region A2-F4 forms a  $\beta$ -strand that is in contact with the CHC and thus the charged NTR residues

**TABLE 4 Average hydrogen bond propensity per residue, showing the five most frequent amino acids involved in intermolecular hydrogen bonding within A $\beta$ 40 and A $\beta$ 42 pentamers and larger oligomers**

A $\beta$ 40				A $\beta$ 42			
$E_{CH} = 0$		$E_{CH} = 0.6$		$E_{CH} = 0$		$E_{CH} = 0.6$	
M35	0.15	M35	0.14	F20	0.18	I31	0.14
I31	0.14	G38	0.14	V18	0.15	G33	0.13
V36	0.14	I31	0.13	G33	0.13	V40	0.13
G37	0.14	G33	0.122	I41	0.13	L17	0.12
G38	0.13	G37	0.12	A21	0.12	F20	0.12

Each value is an average of over 50 conformations at 8, 8.5, 9, 9.5, and 10 million simulation steps.



**FIGURE 10** Intramolecular hydrogen bond maps of A $\beta$ 40 and A $\beta$ 42 pentamers and larger oligomers at  $E_{CH} = 0$  and  $E_{CH} = 0.6$ . Each map is an average of  $>50$  conformations at 8, 8.5, 9, 9.5, and 10 million simulation steps.

(E3 and R5) are interacting with the charged residues K16 and E22, preventing R5-E11 from interacting and breaking the F4-V12 hydrogen bond.

The intermolecular hydrogen bonds of A $\beta$ 40 (Fig. 11, *a* and *b*) and A $\beta$ 42 (Fig. 11, *c* and *d*) pentamers and larger oligomers in the absence (Fig. 11, *a* and *c*) and presence (Fig. 11, *b* and *d*) of EIs are presented. These intermolecular contact maps are normalized to the highest value of intermolecular

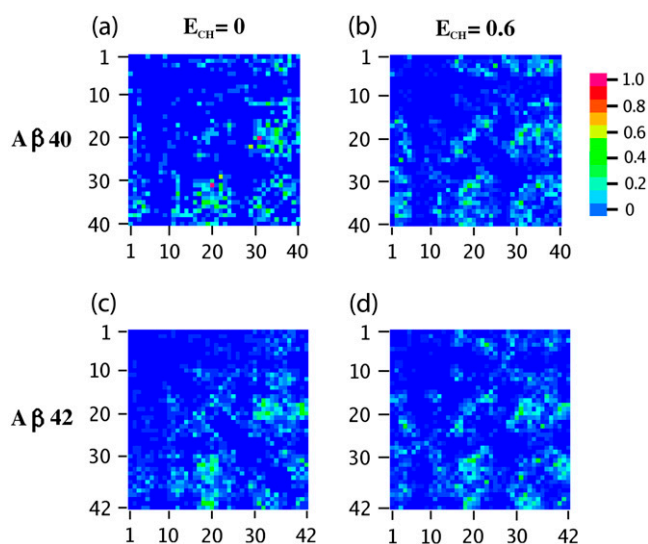


**FIGURE 11** Intermolecular hydrogen bond maps of A $\beta$ 40 and A $\beta$ 42 pentamers and larger oligomers at  $E_{CH} = 0$  and  $E_{CH} = 0.6$ . Each map is an average of  $>50$  conformations at 8, 8.5, 9, 9.5, and 10 million simulation steps.

hydrogen-bond probability, which is  $<0.04$ . The probability of intermolecular hydrogen bond formation is slightly higher in the regions where the contacts are more pronounced. EIs do not influence the intermolecular hydrogen bond formation in any significant way.

Our results show that the hydrogen bonds present in A $\beta$  pentamers and larger oligomers are not specific, indicating that oligomers are not characterized by any particular pattern of hydrogen bonding. These findings suggest that hydrogen bonding is mostly a secondary effect occurring as a consequence of hydrophobic contact formation in the regions CHC, MHR, and CTR.

## CONCLUSIONS

Because molecular dynamics approach to study proteins using all-atom representation and explicit solvent is limited to timescales smaller than  $\sim 10^{-6}$  s, we use a simplified but efficient DMD approach combined with a four-bead protein model and amino-acid-specific interactions that mimic the effects of a solvent (11). In our prior work we showed that this approach yields biologically relevant results, which are consistent with existing experimental findings on A $\beta$  oligomer formation and have predictive power allowing for in vitro and further in silico testing (32). In the present work we use the DMD approach to study the effects of EIs on oligomer formation of A $\beta$ 40 and A $\beta$ 42. The role of electrostatic interactions, in particular the salt-bridge formation between negatively charged E22/D23 and positively charged K28 was hypothesized to be important at early stages of folding as well as at later stages of fibril formation. Thus, it is reasonable to expect that EIs may play an important role at intermediate stages of oligomer formation.

We analyze the structure of folded A $\beta$ 40 and A $\beta$ 42 monomers in the presence and absence of EIs. We show that independent of EIs the two alloforms display differences in folded structure: in A $\beta$ 42 there is an additional turn centered at G37-G38 that is absent in A $\beta$ 40, leading to an increased propensity to form  $\beta$ -strand in the CTR of only A $\beta$ 42. A $\beta$ 40 monomers also have an additional  $\beta$ -strand in the A2-F4, which is not present in A $\beta$ 42. Our results demonstrate that the differences between the two alloforms are present already at the stage of folding, before assembly. The existence of a turn structure centered at G37-G38 is consistent with experimental findings by Lazo et al. (41) who showed by using limited proteolysis that Val<sup>39</sup>-Val<sup>40</sup> in A $\beta$ 42 but not in A $\beta$ 40 monomer was protease-resistant, indicating that A $\beta$ 42 but not A $\beta$ 40 monomer was structured in the CTR region. Similar was a conclusion of the solution NMR study on [Met(O)<sup>35</sup>]A $\beta$ 40 versus [Met(O)<sup>35</sup>]A $\beta$ 42 monomer structure by Riek et al. (63), showing that G29-A42 region is less flexible and thus more structured in A $\beta$ 42 than in A $\beta$ 40. By measuring <sup>1</sup>H <sub>$\alpha$</sub> , <sup>13</sup>C <sub>$\alpha$</sub> , and <sup>13</sup>C <sub>$\beta$</sub>  chemical shift indices of A $\beta$ 40 and A $\beta$ 42, Hou et al. (64) recently showed that the C-terminus of A $\beta$ 42 but not of A $\beta$ 40 monomer has a

tendency to form  $\beta$ -sheet structure, which provides further evidence that our simulation approach yields biologically relevant results consistent with in vitro findings.

Our results indicate that EIs stabilize a turn in the region D23-K28 by formation of a D23-K28 salt bridge. A role for EIs in stabilizing this region has been postulated by Lazo et al. (41) and further explored using a more complex united-atom DMD model (43) and all-atom MD in explicit (44) and implicit solvent (29). These studies show that A $\beta$  folding in the region A21-A30 is driven primarily by effective hydrophobic attraction between V24 and the butyl portion of K28, but that EIs help stabilize the region. In our model, due to its simplicity, the side chains of V24 and K28 do not experience attractive interactions. Despite the absence of this interaction, we still find this region to be the most structured in both A $\beta$ 40 and A $\beta$ 42 monomers stabilized by D23-K28 salt bridge. The D23-K28 salt bridge was suggested to stabilize the A $\beta$ 40 fibril structure by Petkova et al. (46). In addition, Sciarretta et al. (47) have shown an increase in the rate of A $\beta$ 40-Lactam (D23/K28) fibrillogenesis by 1000-fold, providing additional experimental evidence supporting a critical role of D23-K28 salt bridge formation.

Comparing the oligomer size distributions of A $\beta$ 40 and A $\beta$ 42 in the presence of EIs with those obtained in the absence of EIs (32) reveals that EIs promote formation of larger oligomers while maintaining a unimodal A $\beta$ 40 size distribution and a multimodal A $\beta$ 42 size distribution, as observed in vitro (7). In our simulations the N- and C-termini are uncharged in contrast to most experimental studies with positively charged N- and negatively charged C-termini. Our observation that EIs promote formation of larger oligomers is thus consistent with results of the experimental study in which the C-terminal carboxyl group was replaced by the electrostatically neutral carboxamide, resulting in a greater abundance of high molecular weight oligomers (42).

It is critical to study the structural changes in oligomers due to EIs and understand which structural changes are contributing to formation of larger oligomers in both A $\beta$ 40 and A $\beta$ 42. Our results indicate that in A $\beta$ 40 pentamers and larger oligomers, EIs weaken intramolecular interactions. In A $\beta$ 42, in contrast, the intramolecular contacts in the turn region D23-K28 are enhanced. Surprisingly, in both A $\beta$ 40 and A $\beta$ 42 oligomers, the intermolecular contacts involving the CHC are significantly weaker in the presence of EIs. In addition, in A $\beta$ 42 oligomers, the contacts involving the CTR and MHR get stronger. These results, combined with the fact that EIs promote larger oligomers, imply that the intermolecular interactions between pairs of CHCs in an indirect way oppose the formation of larger oligomers, while the interactions between pairs of CTRs, and to a smaller extent also pairs of MHRs, promote formation of larger oligomers. Thus, therapeutic strategies using inhibitors that target the CTR and MHR may prove successful in either inhibiting formation of toxic A $\beta$ 42 oligomers or inducing structural modifications neutralizing their toxicity.

This work was supported by grants from the National Institutes of Health (No. AG023661, No. NS44147, No. NS38328, No. AG18921, and No. AG027818), grant No. A04084 from the American Federation for Aging Research, grant No. 2005/2E from the Larry L. Hillblom Foundation, an Alzheimer's Association Zenith Fellows award, and the Petroleum Research Fund. We are thankful to Stephen Bechtel, Jr. for a private donation.

## REFERENCES

- Hardy, J., and D. J. Selkoe. 2002. The amyloid hypothesis of Alzheimer's disease: progress and problems on the road to therapeutics. *Science*. 297:353–356.
- Kirkitadze, M. D., G. Bitan, and D. B. Teplow. 2002. Paradigm shifts in Alzheimer's disease and other neurodegenerative disorders: the emerging role of oligomeric assemblies. *J. Neurosci. Res.* 69:567–577.
- Klein, W. L., W. B. Stine, and D. B. Teplow. 2004. Small assemblies of unmodified amyloid  $\beta$ -protein are the proximate neurotoxin in Alzheimer's disease. *Neurobiol. Aging*. 25:569–580.
- Sawamura, N., M. Morishima-Kawashima, H. Waki, K. Kobayashi, T. Kuramochi, M. P. Frosch, K. Ding, M. Ito, T. W. Kim, R. E. Tanzi, F. Oyama, T. Tabira, S. Ando, and Y. Ihara. 2000. Mutant presenilin 2 transgenic mice. A large increase in the levels of A $\beta$ 42 is presumably associated with the low density membrane domain that contains decreased levels of glycerophospholipids and sphingomyelin. *J. Biol. Chem.* 275:27901–27908.
- Jarrett, J. T., E. P. Berger, and P. T. J. Lansbury. 1993. The carboxy terminus of the  $\beta$  amyloid protein is critical for the seeding of amyloid formation: implications for the pathogenesis of Alzheimer's disease. *Biochemistry*. 32:4693–4697.
- Jarrett, J. T., E. P. Berger, and P. T. J. Lansbury. 1993. The C-terminus of the  $\beta$  protein is critical in amyloidogenesis. *Ann. N. Y. Acad. Sci.* 695:144–148.
- Bitan, G., M. D. Kirkitadze, A. Lomakin, S. S. Vollers, G. B. Benedek, and D. B. Teplow. 2003. Amyloid  $\beta$ -protein (A $\beta$ ) assembly: A $\beta$ 40 and A $\beta$ 42 oligomerize through distinct pathways. *Proc. Natl. Acad. Sci. USA*. 100:330–335.
- Walsh, D. M., A. Lomakin, G. B. Benedek, M. M. Condron, and D. B. Teplow. 1997. Amyloid  $\beta$ -protein fibrillogenesis—detection of a protofibrillar intermediate. *J. Biol. Chem.* 272:22364–22372.
- Teplow, D., N. Lazo, G. Bitan, S. Bernstein, T. Wyttenbach, M. Bowers, A. Baumketner, J.-E. Shea, B. Urbanc, L. Cruz, J. Borreguero, and H. E. Stanley. 2006. Elucidating amyloid  $\beta$ -protein folding and assembly: a multidisciplinary approach. *Acc. Chem. Res.* 39:635–645.
- Urbanc, B., L. Cruz, D. B. Teplow, and H. E. Stanley. 2006. Computer simulations of Alzheimer's amyloid  $\beta$ -protein folding and assembly. *Curr. Alzheimer Res.* 3:493–504.
- Urbanc, B., J. Borreguero, L. Cruz, and H. E. Stanley. 2006. *Ab initio* discrete molecular dynamics approach to protein folding and aggregation. *Methods Enzymol.* 412:314–338.
- Klimov, D. K., and D. Thirumalai. 2003. Dissecting the assembly of A $\beta$ <sub>16–22</sub> amyloid peptides into antiparallel  $\beta$  sheets. *Structure*. 11: 295–307.
- Tarus, B., J. E. Straub, and D. Thirumalai. 2005. Probing the initial stage of aggregation of the A $\beta$ <sub>10–35</sub>-protein: assessing the propensity for peptide dimerization. *J. Mol. Biol.* 345:1141–1156.
- Huet, A., and P. Derreumaux. 2006. Impact of the mutation A21G (Flemish variant) on Alzheimer's  $\beta$ -amyloid dimers by molecular dynamics simulations. *Biophys. J.* 91:3829–3840.
- Rapaport, D. C. 1997. *The Art of Molecular Dynamics Simulation*. Cambridge University Press, Cambridge, UK.
- Teplow, D. B., N. D. Lazo, G. Bitan, S. Bernstein, T. Wyttenbach, M. T. Bowers, A. Baumketner, J.-E. Shea, B. Urbanc, L. Cruz, J. Borreguero, and H. E. Stanley. 2006. Elucidating amyloid  $\beta$ -protein folding and assembly: a multidisciplinary approach. *Acc. Chem. Res.* 39:635–645.
- Zhou, Y., C. K. Hall, and M. Karplus. 1996. First-order disorder-to-order transition in an isolated homopolymer model. *Phys. Rev. Lett.* 77:2822–2825.
- Dokholyan, N. V., S. V. Buldyrev, H. E. Stanley, and E. I. Shakhnovich. 1998. Discrete molecular dynamics studies of the folding of a protein-like model. *Fold. Des.* 3:577–587.
- Dokholyan, N. V., S. V. Buldyrev, H. E. Stanley, and E. I. Shakhnovich. 2000. Identifying the protein folding nucleus using molecular dynamics. *J. Mol. Biol.* 296:1183–1188.
- Zhou, Y. Q., and M. Karplus. 1997. Folding thermodynamics of a model three-helix-bundle protein. *Proc. Natl. Acad. Sci. USA*. 94: 14429–14432.
- Zhou, Y. Q., M. Karplus, J. M. Wichert, and C. K. Hall. 1997. Equilibrium thermodynamics of homopolymers and clusters: molecular dynamics and Monte Carlo simulations of systems with square-well interactions. *J. Chem. Phys.* 107:10691–10708.
- Zhou, Y. Q., and M. Karplus. 1999. Folding of a model three-helix bundle protein: a thermodynamic and kinetic analysis. *J. Mol. Biol.* 293:917–951.
- Peng, S., F. Ding, B. Urbanc, S. V. Buldyrev, L. Cruz, H. E. Stanley, and N. V. Dokholyan. 2004. Discrete molecular dynamics simulations of peptide aggregation. *Phys. Rev. E*. 69:041908.
- Smith, A. V., and C. K. Hall. 2001. Alpha-helix formation: discontinuous molecular dynamics on an intermediate-resolution protein model. *Proteins Struct. Funct. Genet.* 44:344–360.
- Smith, A. V., and C. K. Hall. 2001. Assembly of a tetrameric  $\alpha$ -helical bundle: computer simulations on an intermediate-resolution protein model. *Proteins Struct. Funct. Genet.* 44:376–391.
- Ding, F., J. M. Borreguero, S. V. Buldyrev, H. E. Stanley, and N. V. Dokholyan. 2003. Mechanism for the  $\alpha$ -helix to  $\beta$ -hairpin transition. *Proteins Struct. Funct. Genet.* 53:220–228.
- Urbanc, B., L. Cruz, F. Ding, D. Sammond, S. Khare, S. V. Buldyrev, H. E. Stanley, and N. V. Dokholyan. 2004. Molecular dynamics simulation of amyloid  $\beta$  dimer formation. *Biophys. J.* 87:2310–2321.
- Lam, A., B. Urbanc, J. M. Borreguero, N. D. Lazo, D. B. Teplow, and H. E. Stanley. 2006. Discrete molecular dynamics study of Alzheimer amyloid  $\beta$ -protein (A $\beta$ ) folding. Proceedings of the 2006 International Conference on Bioinformatics and Computational Biology. 322–328.
- Baumketner, A., S. L. Bernstein, T. Wyttenbach, G. Bitan, D. B. Teplow, M. T. Bowers, and J.-E. Shea. 2006. Amyloid  $\beta$ -protein monomer structure: a computational and experimental study. *Protein Sci.* 15:420–428.
- Gursky, O., and S. Aleshkov. 2000. Temperature-dependent  $\beta$ -sheet formation in  $\beta$ -amyloid A $\beta$ (1–40) peptide in water: uncoupling  $\beta$ -structure folding from aggregation. *Biochim. Biophys. Acta*. 1476: 93–102.
- Lim, K. H., H. H. Collver, Y. T. H. Le, P. Nagchowdhuri, and J. M. Kenney. 2007. Characterizations of distinct amyloidogenic conformations of the A $\beta$  (1–40) and (1–42) peptides. *Biochem. Biophys. Res. Commun.* 353:443–449.
- Urbanc, B., L. Cruz, S. Yun, S. V. Buldyrev, G. Bitan, D. B. Teplow, and H. E. Stanley. 2004. *In silico* study of amyloid  $\beta$ -protein folding and oligomerization. *Proc. Natl. Acad. Sci. USA*. 101:17345–17350.
- Bernstein, S. L., T. Wyttenbach, A. Baumketner, J.-E. Shea, G. Bitan, D. B. Teplow, and M. T. Bowers. 2005. Amyloid  $\beta$ -protein: monomer structure and early aggregation states of A $\beta$ 42 and its Pro19 alloform. *J. Am. Chem. Soc.* 127:2075–2084.
- Gong, Y. S., L. Chang, K. L. Viola, P. N. Lacor, M. P. Lambert, C. E. Finch, G. A. Krafft, and W. L. Klein. 2003. Alzheimer's disease-affected brain: presence of oligomeric A $\beta$  ligands (ADDLs) suggests a molecular basis for reversible memory loss. *Proc. Natl. Acad. Sci. USA*. 100:10417–10422.
- Barghorn, S., V. Nimmrich, A. Striebinger, C. Krantz, P. Keller, B. Janson, M. Bahr, M. Schmidt, R. S. Bitner, J. Harlan, E. Barlow, U. Ebert, and H. Hillen. 2005. Globular amyloid  $\beta$ -peptide oligomer—a homogenous and stable neuropathological protein in Alzheimer's disease. *J. Neurochem.* 95:834–847.

36. Lesne, S., M. T. Koh, L. Kotilinek, R. Kaye, C. G. Glabe, A. Yang, M. Gallagher, and K. H. Ashe. 2006. A specific amyloid- $\beta$  protein assembly in the brain impairs memory. *Nature*. 440:352–357.
37. Bitan, G., B. Tarus, S. S. Vollers, H. A. Lashuel, M. M. Condron, J. E. Straub, and D. B. Teplow. 2003. A molecular switch in amyloid assembly: Met<sup>35</sup> and amyloid  $\beta$ -protein oligomerization. *J. Am. Chem. Soc.* 125:15359–15365.
38. Seilheimer, B., B. Bohrmann, L. Bondolfi, F. Muller, D. Stuber, and H. Dobeli. 1997. The toxicity of the Alzheimer's  $\beta$ -amyloid peptide correlates with a distinct fiber morphology. *J. Struct. Biol.* 119:59–71.
39. Snyder, S. W., U. S. Lador, W. S. Wade, G. T. Wang, L. W. Barrett, E. D. Matayoshi, H. J. Huffaker, G. A. Krafft, and T. F. Holzman. 1994. Amyloid- $\beta$  aggregation: selective inhibition of aggregation in mixtures of amyloid with different chain lengths. *Biophys. J.* 67:1216–1228.
40. Watson, A. A., D. P. Fairlie, and D. J. Craik. 1998. Solution structure of methionine-oxidized amyloid  $\beta$ -peptide (1–40). Does oxidation affect conformational switching? *Biochemistry*. 37:12700–12706.
41. Lazo, N. D., M. A. Grant, M. C. Condron, A. C. Rigby, and D. B. Teplow. 2005. On the nucleation of amyloid  $\beta$ -protein monomer folding. *Protein Sci.* 14:1581–1596.
42. Bitan, G., S. Vollers, and D. B. Teplow. 2003. Elucidation of primary structure elements controlling early amyloid  $\beta$ -protein oligomerization. *J. Biol. Chem.* 278:34882–34889.
43. Borreguero, J. M., B. Urbanc, N. D. Lazo, S. V. Buldyrev, D. B. Teplow, and H. E. Stanley. 2005. Folding events in the 21–30 region of amyloid  $\beta$ -protein (A $\beta$ ) studied *in silico*. *Proc. Natl. Acad. Sci. USA*. 102:6015–6020.
44. Cruz, L., B. Urbanc, J. M. Borreguero, N. D. Lazo, D. B. Teplow, and H. E. Stanley. 2005. Solvent and mutation effects on the nucleation of amyloid  $\beta$ -protein folding. *Proc. Natl. Acad. Sci. USA*. 102:18258–18263.
45. Petkova, A. T., W.-M. Yau, and R. Tycko. 2006. Experimental constraints on quaternary structure in Alzheimer's  $\beta$ -amyloid fibrils. *Biochemistry*. 45:498–512.
46. Petkova, A. T., Y. Ishii, J. J. Balbach, O. N. Antzutkin, R. D. Leapman, F. Delaglio, and R. Tycko. 2002. A structural model for Alzheimer's  $\beta$ -amyloid fibrils based on experimental constraints from solid state NMR. *Proc. Natl. Acad. Sci. USA*. 99:16742–16747.
47. Sciarretta, K. L., D. J. Gordon, A. T. Petkova, R. Tycko, and S. C. Meredith. 2005. A $\beta$ 40-Lactam(D23/K28) models a conformation highly favorable for nucleation of amyloid. *Biochemistry*. 44:6003–6014.
48. Kyte, J., and R. F. Doolittle. 1982. A simple method for displaying the hydropathic character of a protein. *J. Mol. Biol.* 157:105–132.
49. Sheu, S.-Y., D.-Y. Yang, H. L. Selzle, and E. W. Schlag. 2003. Energetics of hydrogen bonds in peptides. *Proc. Natl. Acad. Sci. USA*. 100:12683–12687.
50. Luisi, D. L., C. D. Snow, J.-J. Lin, Z. S. Hendsch, B. Tidor, and D. P. Raleigh. 2003. Surface salt bridges, double-mutant cycles, and protein stability: an experimental and computational analysis of the interaction of the Asp-23 side chain with the N-terminus of the N-terminal domain of the ribosomal protein L9. *Biochemistry*. 42:7050–7060.
51. Berendsen, H. J. C., J. Postma, W. V. Gunsteren, A. DiNola, and J. Haak. 1984. Molecular dynamics with coupling to an external bath. *J. Chem. Phys.* 81:3684–3690.
52. Bradley, P., L. Malmstrom, B. Qian, J. Schonbrun, D. Chivian, D. E. Kim, J. Meiler, K. M. S. Misura, and D. Baker. 2005. Free modeling with Rosetta in CASP6. *Proteins*. 61:128–134.
53. Baker, D. 2000. A surprising simplicity to protein folding. *Nature*. 405:39–42.
54. Dobson, C. M. 2004. Experimental investigation of protein folding and misfolding. *Methods*. 34:4–14.
55. Bowie, J. U., R. Luthy, and D. Eisenberg. 1991. A method to identify protein sequences that fold into a known three-dimensional structure. *Science*. 253:164–170.
56. Finkelstein, A. V., and B. A. Reva. 1991. A search for the most stable folds of protein chains. *Nature*. 351:497–499.
57. Nguyen, H. D., and C. K. Hall. 2006. Spontaneous fibril formation by polyalanines: discontinuous molecular dynamics simulations. *J. Am. Chem. Soc.* 128:1890–1901.
58. Press, W. H., S. A. Teukolsky, W. T. Vetterling, and B. P. Flannery. 1992. *Numerical Recipes in FORTRAN: The Art of Scientific Computing*, 2nd Ed. Cambridge University Press, Cambridge, UK.
59. Heinig, M., and D. Frishman. 2004. STRIDE: a web server for secondary structure assignment from known atomic coordinates of proteins. *Nucleic Acids Res.* 32:500–502.
60. Zhang, S., K. Iwata, M. J. Lachenmann, J. W. Peng, S. Li, E. R. Stimson, Y. Lu, A. M. Felix, J. E. Maggio, and J. P. Lee. 2000. The Alzheimer's peptide A $\beta$  adopts a collapsed coil structure in water. *J. Struct. Biol.* 130:130–141.
61. Lasic, D., L. L. Martin, A. Mechler, M.-I. Aguilar, and D. H. Small. 2006. High resolution scanning tunneling microscopy of the  $\beta$ -amyloid protein (A $\beta$ 1–40) of Alzheimer's disease suggests a novel mechanism of oligomer assembly. *J. Struct. Biol.* 155:104–110.
62. Maji, S. K., J. J. Amsden, K. J. Rothschild, M. M. Condron, and D. B. Teplow. 2005. Conformational dynamics of amyloid  $\beta$ -protein assembly probed using intrinsic fluorescence. *Biochemistry*. 44:13365–13376.
63. Riek, R., P. Guntert, H. Dobeli, B. Wipf, and K. Wuthrich. 2001. NMR studies in aqueous solution fail to identify significant conformational differences between the monomeric forms of two Alzheimer peptides with widely different plaque-competence, A $\beta$ (1–40)<sup>(ox)</sup> and A $\beta$ (1–42)<sup>(ox)</sup>. *Eur. J. Biochem.* 268:5930–5936.
64. Hou, L., H. Shao, Y. Zhang, H. Li, N. K. Menon, E. B. Neuhuis, J. M. Brewer, I. L. Byeon, D. G. Ray, M. P. Vitek, T. Iwashita, R. A. Makula, A. B. Przybyla, and M. G. Zagorski. 2004. Solution NMR studies of the A $\beta$ (1–40) and A $\beta$ (1–42) peptides establish that the Met<sup>35</sup> oxidation state affects the mechanism of amyloid formation. *J. Am. Chem. Soc.* 126:1992–2005.
65. Humphrey, W., A. Dalke, and K. Schulten. 1996. VMD: visual molecular dynamics. *J. Mol. Graph.* 14:33–38.